Chemical Science

ROYAL SOCIETY OF CHEMISTRY

EDGE ARTICLE

View Article Online
View Journal | View Issue



Cite this: *Chem. Sci.*, 2024, **15**, 13853

All publication charges for this article have been paid for by the Royal Society of Chemistry

Received 22nd June 2024
Accepted 25th July 2024

DOI: 10.1039/d4sc04125a

rsc.li/chemical-science



# Realizing altermagnetism in two-dimensional metal–organic framework semiconductors with electric-field-controlled anisotropic spin current†

Yixuan Che, [a] Haifeng Lv, *[b] Xiaojun Wu *[bc] and Jinlong Yang [abc]

Altermagnets exhibit momentum-dependent spin-splitting in a collinear antiferromagnetic order due to their peculiar crystallographic and magnetic symmetry, resulting in the creation of spin currents with light elements. Here, we report two two-dimensional (2D) metal–organic framework (MOF) semiconductors, $M(pyz)_2$ (M = Ca and Sr, pyz = pyrazine), which exhibit both altermagnetism and topological nodal point and line by using first-principles calculations and group theory. The altermagnetic 2D MOFs exhibit unconventional spin-splitting and macroscopic zero magnetization caused by 4-fold rotation in crystalline real space and 2-fold rotation in spin space, leading to the generation and control of anisotropic spin currents when an in-plane electric field (***E***) is applied. In particular, pure spin current with the spin Hall effect occurs when ***E*** is applied along the angular bisector of the two spin arrangements. Our work indicates the existence of altermagnetic MOF systems and a universal approach to generate electric-field-controlled spin currents for potential applications in antiferromagnetic spintronics.

## Introduction

Spintronics, using only the spin freedom of electrons to store, transport, and process information, offers the opportunity to reduce the generation of Joule heat in conventional electronics by utilizing spin alignment.[1] There are two primary phases of spin alignment in the collinear form, *i.e.*, ferromagnetic and antiferromagnetic order with the spins aligned in parallel and antiparallel directions, respectively. Ferromagnets are disturbed by the stray fields and antiferromagnets are normally absent of spin-splitting in energy bands, posing a formidable challenge in their practical applications in spintronics.[2] In addition, the generation of pure spin current in spintronics as a substitute for electron current is highly desirable due to its potential for reduced power consumption, but it still faces big challenges.

Recently, altermagnets that exhibit a spontaneous spin-splitting of energy bands and lack macroscopic magnetism in the collinear antiferromagnetic form have been proposed based on crystalline and magnetic symmetry.[3–6] Compared to conventional antiferromagnets, altermagnets possess unique characteristics, including unconventional spin-splitting due to the valley-dependent spin–momentum coupling, as well as adjustable charge and spin currents through anisotropic spin–momentum coupling.[7] These features make them suitable for various applications such as spintronics,[7,8] thermo-electric response,[9] field-effect electronics,[10] multiferroics,[11] superconductivity,[12] *etc*. For example, the rutile metal $RuO_2$ bulk shows unconventional broken time-reversal ($T$) symmetry transport anomalies and spintronic effects, including the anomalous Hall effect,[13–15] charge–spin conversion,[8,16] spin-torque phenomena,[17–19] and giant and tunneling magnetoresistance.[7,20] By doping, insulating perovskite $La_2CuO_4$ transforms into a high-temperature $d$-wave superconductor.[3,21] Two-dimensional (2D) $V_2Se_2O$ crystal is a multifunctional inorganic material that displays giant piezomagnetism, which enables manipulation of both spin and valley.[22] Furthermore, 2D CrO crystal exhibits large spin-splitting and spin–momentum-locked transport, together with a high magnetic transition temperature.[23] Theoretically, high-throughput screening from existing databases has enriched the quantity of altermagnets in both 2D and 3D systems.[24–26] Experimentally, spin-splitting in altermagnets can be detected from photoemission spectroscopy and ARPES measurements.[27–29] However, it is highly desirable to explore experimentally feasible altermagnets in the nanoscale that are beyond the limiting range of existing inorganic altermagnetic materials.

[a]*Hefei National Research Center for Physical Sciences at the Microscale, University of Science and Technology of China, Hefei, Anhui 230026, China*

[b]*Key Laboratory of Precision and Intelligent Chemistry, CAS Key Laboratory of Materials for Energy Conversion, School of Chemistry and Materials Science, and Collaborative Innovation Center of Chemistry for Energy Materials (iChEM), University of Science and Technology of China, Hefei, Anhui 230026, China. E-mail: hflv@ustc.edu.cn; xjwu@ustc.edu.cn*

[c]*Hefei National Laboratory, University of Science and Technology of China, Hefei, Anhui 230088, China*

† Electronic supplementary information (ESI) available. See DOI: https://doi.org/10.1039/d4sc04125a

Metal–organic frameworks (MOFs), assembled with metal nodes and organic linkers, provide a versatile chemical platform that exhibits peculiar magnetism in 2D forms.[30] By modulating the coordination modes, the spin-related properties of 2D MOFs can be created and regulated. For instance, the orthorhombic $[Fe(pyz)_2(NCS)_2]_n$ (pyz = pyrazine) polymeric sheet shows antiferromagnetic behavior below 8.5 K and the neutron powder diffraction showed a three-dimensional (3D) long-range order below 6.8 K.[31,32] The antiferromagnetic triclinic $M(NCS)_2(pzdo)_2$ (M = Mn or Co, pzdo = pyrazine dioxide) maintain its magnetic order at the temperature below 8.4 and 11.2 K for Mn and Co, respectively.[33] Non-crystal-symmetry compensated magnets, such as the ferromagnetic orthorhombic $Cr(ptl)_2$ (ptl = pentalene),[34] the ferrimagnetic tetragonal $Cr(pyz)_2$,[35–37] and the pentafunctional ferrimagnetic $Cr(tdz)_2$ (tdz = 1,2,5-thiadiazole),[38] have high magnetic transition temperatures of 560, 342, and 378 K, respectively, because of the strong *d–p* direct exchange interaction between the metal and N atoms.

Here, we present two 2D MOF altermagnetic semiconductors, namely $M(pyz)_2$ (M = Ca and Sr), by assembling the alkaline earth metal atoms as nodes and pyrazine (1,4-diazine) as organic linkers based on first-principles calculations. The 2D MOFs exhibit altermagnetism at their ground state, characterized by unconventional spin-splitting and macroscopic zero magnetization caused by the 4-fold rotation ($C_{4z}$) in crystalline real space and 2-fold rotation ($C_2$) in spin space. Particularly, spin current ($\boldsymbol{J}_s$) can be generated and reversely regulated by the in-plane electric field ($\boldsymbol{E}$) direction. The spin Hall effect (SHE)[39] generates pure transverse $\boldsymbol{J}_s$ when $\boldsymbol{E}$ is applied along the angular bisector of two spin configurations.

## Results and discussion

Conventional antiferromagnets lack macroscopic magnetism and have degenerate energy bands due to opposing spin channels, typically displaying similar electric behaviors to nonmagnetic materials. Altermagnet is a novel type of antiferromagnet that exhibits additionally unconventional spin polarization and spin-splitting in reciprocal momentum space, which is determined by specific crystallographic symmetry and magnetic ground state.[3,4,9,13,22,23,27,28,40] As shown in Fig. 1a, in conventional antiferromagnets, opposite-spin sublattices are connected by inversion ($i$) or translation ($t$). These connections can be represented as the notation $[C_2\|i]$ or $[C_2\|t]$, where the transformation on the left side of the double vertical bars affects only the spin space, while the one on the right side affects only the crystalline real space. Spin valleys are isotropic, and sublattices of conventional antiferromagnets belong to the same crystallographic point group **G** as the material. In the case of altermagnets, as shown in Fig. 1b, the $\alpha$ and $\beta$ spins are connected by rotation ($R$), but inversion and translation are prohibited. The spin symmetry notation is denoted as $[C_2\|R]$, and the point group of sublattice **H** is a subgroup of **G** with an index of 2. The $\alpha$ and $\beta$ spin channels in altermagnets are nondegenerate, equally occupied, and anisotropic.

The time-reversal symmetry arises from the multiplication of $[C_2\|\mathbf{X}]$ and the spin-only group symmetry $[C_{2\perp}\|T]$, *i.e.*, $[T\|T\mathbf{X}]$. Here, **X** is a set of symmetric elements, and $C_{2\perp}$ represents a 180° rotation around an axis perpendicular to spins. In conventional antiferromagnets, **X** is the crystalline point group **G** including the identity element ($E$). Thus, the $T$-symmetry is an element of its spin point group and is reflected in the band degeneracy of $\alpha$ and $\beta$ spins (Fig. 1a). In the case of altermagnets, $\mathbf{X} = \mathbf{G} \ominus \mathbf{H}$, where the coset $\mathbf{G} \ominus \mathbf{H}$ does not include $E$. As a result, the $T$-symmetry is broken, leading to the spin-splitting of energy bands and spin polarization in momentum space (Fig. 1b, and see details in ESI Note S1†).

Due to the anisotropic spin channels, the spin current ($\boldsymbol{J}_s = \boldsymbol{J}_\alpha - \boldsymbol{J}_\beta$) in altermagnets can be regulated by directly controlling in-plane $\boldsymbol{E}$ direction. As $\boldsymbol{E}$ rotates, $\boldsymbol{J}_s$ will undergo a rotation in the opposite direction, maintaining the same angle ($\varphi$). When the in-plane $\boldsymbol{E}$ is applied along a certain spin valley configuration of $\alpha$ or $\beta$ (Fig. 1c and d), the spin current will be parallel to the direction of the electric field and will flow in the opposite direction depending on the spin types along which $\boldsymbol{E}$ is applied. When $\boldsymbol{E}$ is applied at the angular bisector of two spin arrangements (Fig. 1e and f), carriers with $\alpha$ and $\beta$ spins will undergo equal deflection but in opposite directions, leading to pure transverse $\boldsymbol{J}_s$ and SHE (see details in ESI Note S2†).[39] Anisotropies, spin-splitting, and spin current in altermagnets arise from their unique symmetries independent of spin–orbit coupling (SOC), enabling their realization in materials containing only light elements.[27,28] The primary rules for identifying altermagnetic phases of crystals have been proposed in previous reports, which serve as a foundation for the rational design of such materials.[3,4]

Benefitting from the abundant ligands, unpaired electrons, and various topologies, it is highly promising to construct MOFs with targeted magnetic order, such as altermagnetism, by selecting the core metal, organic linker, and topology.

### Structure and stabilities

In 2D MOFs, metal atoms are tetra-coordinated with four adjacent pyrazine ligands *via* metal–nitrogen bonds, forming a square plane. The pyrazine ligand exhibits a $C_{4z}$ rotational symmetry with the metal atom as its center (Fig. 2a–c). The $Be(pyz)_2$ and $Mg(pyz)_2$ undergo a phase transition from tetragonal to orthorhombic, which is caused by the small radius of alkaline earth metal atoms, the significant steric hindrance between hydrogen atoms in neighboring pyrazine ligands, and a substantial torsion angle along the Be(Mg)–N bonds. However, $Ca(pyz)_2$, $Sr(pyz)_2$, and $Ba(pyz)_2$ can exhibit tetragonal phases with the space group of *P*4/*nbm* (#125). The calculated lattice parameters, bond lengths between the metal and N atoms, sheet thicknesses, torsion angles, Bader charge transfer from the metal atoms to pyrazine ligands, formation energies per stoichiometric formula, and electronic band gaps are summarized in Table 1. The lattice parameters and bond lengths between metal and nitrogen atoms increase when the period of metal atoms increases, while torsion angles and monolayer thicknesses decrease.

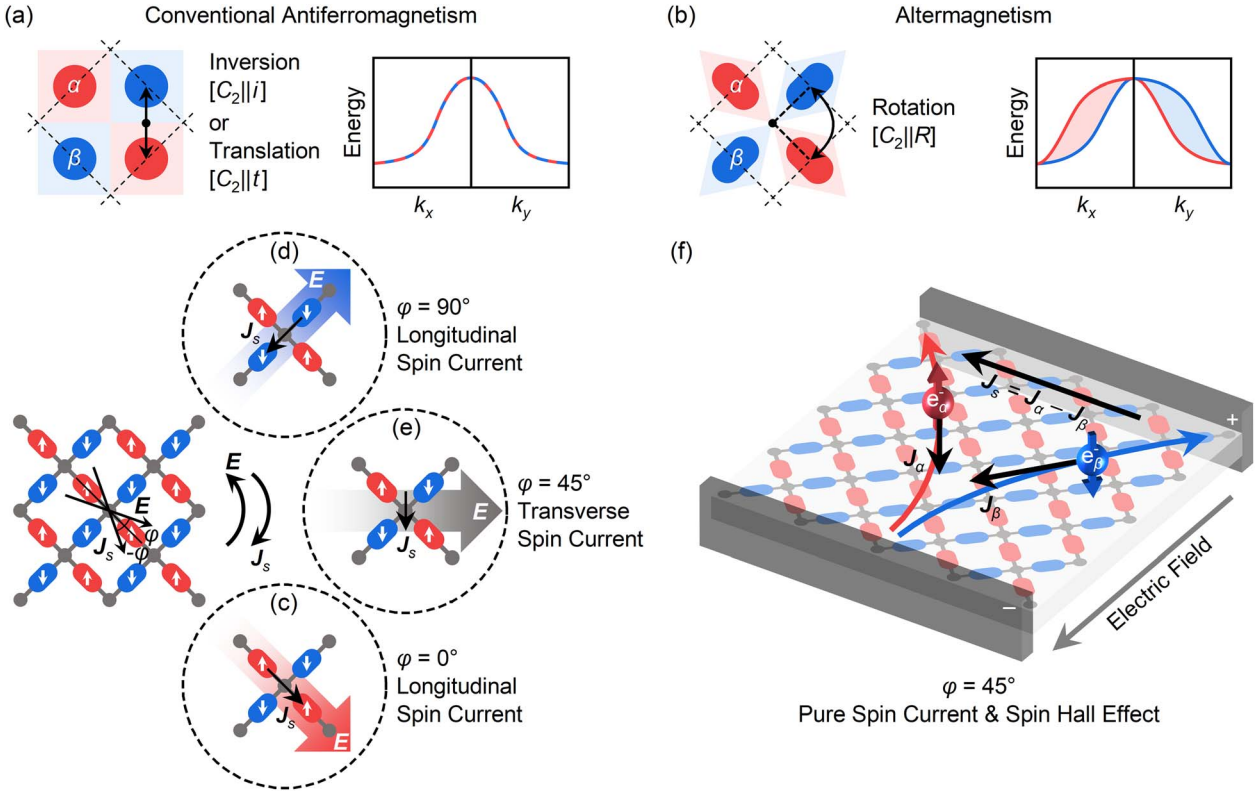


Fig. 1 Characteristics of altermagnetism and schematic illustrations of the anisotropic spin current ($J_s$) regulation. (a) Opposite-spin sublattices (light-colored quadrilaterals, same below) in conventional antiferromagnets are connected by inversion ($i$) or translation ($t$) and spin valleys are isotropic (left panel), which is reflected in the band degeneracy of $\alpha$ and $\beta$ spins (right panel). (b) For altermagnets, opposite-spin sublattices are connected by rotation ($R$) rather than inversion and spin valleys are anisotropic (left panel), which is reflected in the spin-splitting of energy bands (right panel). In altermagnets, $J_s$ can be directly regulated by the in-plane electric field ($E$) direction due to the anisotropic spin channels, and as $E$ rotates, $J_s$ will rotate in the opposite direction at the same angle ($\varphi$). (c and d) When the electric field follows the direction of a certain spin arrangement, longitudinal spin currents will appear and exhibit opposite directions under different spins. (e and f) When the electric field follows the angular bisector of two spin arrangements, pure transverse $J_s$ with no Hall charge current will be observed, and the charge–spin conversion ratio will reach maximum. The carriers with $\alpha$ and $\beta$ spins undergo the same degree of deflection but in opposite directions under the in-plane $E$ on the angular bisector, resulting in the spin Hall effect (SHE). Particularly, for the altermagnetic M(pyz)$_2$ (M = Ca and Sr) with $C_{4z}$ rotation between sublattices, the longitudinal and transverse $J_s$ will alternate in cycles of 45°, and the pure transverse $J$ and SHE will appear at $\varphi = 45°$. Red and blue denote opposite spins. Dashed boxes in (a) and (b) are the unit cells in spin space.

To examine the stability of 2D MOFs, the average formation energy per stoichiometric formula ($\mathscr{E}_{\text{form}}$) of the two thermally stable sheets is calculated using the following equation:

$$\mathscr{E}_{\text{form}} = \frac{\mathscr{E}_{\text{MOF}} - \left(2\mathscr{E}_{\text{M}} + 4\mathscr{E}_{\text{pyz}}\right)}{2}, \quad (1)$$

where $\mathscr{E}_{\text{MOF}}$, $\mathscr{E}_{\text{M}}$, and $\mathscr{E}_{\text{pyz}}$ denote the energies of 2D MOFs, metal atoms, and pyrazine rings, respectively. Table 1 provides a summary of the calculated energies, which vary from −4.11 to −4.65 eV. These values indicate that the synthesis of three altermagnetic 2D MOFs using metal atoms and pyrazine ligands is feasible. As shown in Fig. S1,† temperature, reaction time, solvent, and additive conditions can be predicted by the MOF Synthesis Prediction Tool.[41] It is shown that water is predicted as the solvent with neutral or no additive for 2D MOFs with high certainty, while temperature and reaction time are predicted with medium certainty. Furthermore, the Bader charge transfer from the metal atoms to pyrazine ligands increases as the period of metal atoms increases, correlating to their electronegativities (Table 1).

The structural dynamical stability of 2D MOFs is examined by the calculated phonon spectrum. Fig. S2† shows the absence of imaginary frequencies in the phonon spectra of Ca(pyz)$_2$ and Sr(pyz)$_2$, indicating that they are dynamically stable. On the other hand, Ba(pyz)$_2$ exhibits the presence of soft phonon modes at around 20i cm$^{-1}$, corresponding to the relative vibration of Ba atoms along $c$-axis. This is partly due to the large atomic radius of Ba, which increases the lattice parameter and causes structural instability. Thus, only Ca(pyz)$_2$ and Sr(pyz)$_2$ are studied in the following (Tables S1 and S2†).

The thermal stabilities of the 2D MOFs are analyzed using *ab initio* molecular dynamic (AIMD) simulations. The simulations are performed at 300, 600, and 900 K for 5 ps with a time step of 1 fs. The structural snapshots are shown in Fig. S3 and S4.† 2D MOFs exhibit thermal stability by preserving their structural integrity at a temperature as high as 600 K. Additionally, it is shown that pyrazine rings can easily rotate between the metal nodes. To verify the stability with different torsion angles, the PBE self-consistent-field energies with different torsion angles

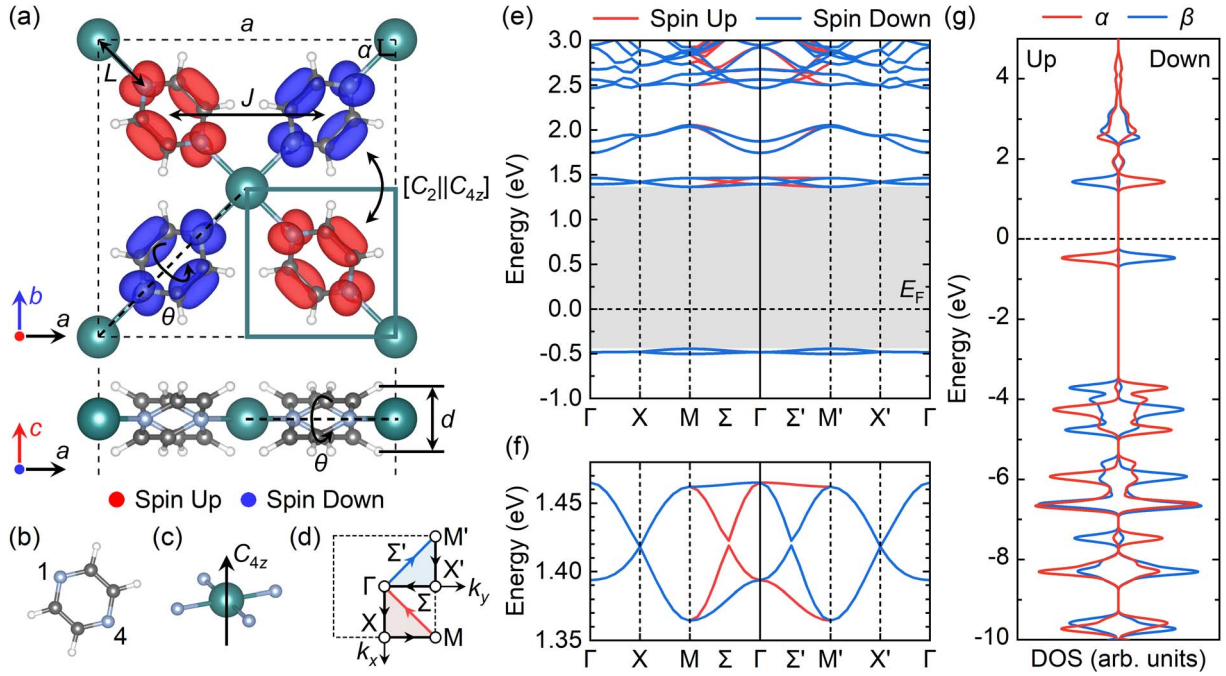


Fig. 2 Altermagnetic 2D $Ca(pyz)_2$ with unconventional spin-splitting and valley-dependent spin-polarized sublattices. (a–c) Structure and spin valleys of the altermagnetic 2D $Ca(pyz)_2$. (a) The *P*4/*nbm* (#125) $Ca(pyz)_2$ is connected by (b) the pyrazine (1,4-diazine) ligands and Ca atoms with (c) Ca–N tetra-coordination, where the sublattices with different spins obtain the $C_{4z}$ rotational symmetry in the planar square field. The isosurface value of spin density in (a) is 0.005 e bohr$^{-3}$, where the red and blue colors represent up and down spins, respectively. Green, gray, blue, and white balls represent Ca, C, N, and H atoms, respectively. Structural parameters in Table 1 are labeled in (a). (d) The first Brillouin zone (BZ) of the altermagnetic 2D $Ca(pyz)_2$ with high symmetry *k*-points and *k*-paths. The red and blue arrows represent the different spin-splitting paths and the corresponding triangle areas are the two irreducible parts of the first BZ. (e) Band structure of the altermagnetic 2D $Ca(pyz)_2$ with HSE06 functional *via* the *k*-path in (d), with (f) spin-splitting of the bands around CBM. The gray shadows in (e) represent the band gap ($\mathscr{E}_g = 1.81$ eV). (g) Sublattice and spin resolved density of states (DOS) of the altermagnetic 2D $Ca(pyz)_2$. The $\alpha$ sublattice is framed with solid green lines in (a) while the $\beta$ lattice is the corresponding opposite one. The Fermi level ($\mathscr{E}_F$) is set to 0 eV.

Table 1 The calculated lattice parameters (*a* for length and $\alpha$ for angle, in Å and °, respectively), bond lengths between metal and N atoms (*L*, in Å), sheet thicknesses (*d*, in Å), torsion angles ($\theta$, in °), Bader charge transfer from the metal atoms to pyrazine ligands (*C*, in e$^-$), formation energies ($\mathscr{E}_{form}$, in eV per stoichiometric formula), and electronic band gaps ($\mathscr{E}_g$, in eV) of the tetragonal $M(pyz)_2$ (M = Ca, Sr, and Ba). The values of $\mathscr{E}_g$ are calculated with HSE06 hybrid functional

| | $Ca(pyz)_2$ | $Sr(pyz)_2$ | $Ba(pyz)_2$ |
|---|---|---|---|
| $a$ | 10.86 | 11.34 | 11.84 |
| $\alpha$ | 90.00 | 90.00 | 90.00 |
| $L$ | 2.39 | 2.56 | 2.74 |
| $d$ | 2.39 | 2.21 | 2.13 |
| $\theta$ | 34.66 | 31.71 | 30.49 |
| $C$ | 1.36 | 1.63 | 1.66 |
| $\mathscr{E}_{form}$ | −4.65 | −4.22 | −4.15 |
| $\mathscr{E}_g$ | 1.81 | 1.79 | 1.70 |

are calculated, as shown in Fig. S5.† It is shown that the relaxed structures are the most stable with an energy minimum to a single value of torsion angles, indicating their stability. The energy variation is relatively small when the torsion angle is between 30° and 90°, corresponding to the pyrazine rotating in AIMD simulations. Additionally, due to the lattice parameter of $Ca(pyz)_2$ being smaller than $Sr(pyz)_2$, the steric hindrance between neighboring pyrazine ligands of flat $Ca(pyz)_2$ is larger, thus with a larger energy difference to the stable phase.

The stress–strain method is used to analyze the mechanical stabilities by calculating the elastic constants. The values of $C_{11}$, $C_{12}$, and $C_{66}$ for $Ca(pyz)_2$ are 21.85, 21.63, and 17.61 N m$^{-1}$. For $Sr(pyz)_2$, the values are 15.91, 14.00, and 15.10 N m$^{-1}$, respectively. Both $Ca(pyz)_2$ and $Sr(pyz)_2$ are mechanically stable, confirmed by their elastic constants (see details in Methods).[42]

## Altermagnetism and magnetic transition temperature

The magnetic ground states of 2D MOFs are determined by considering several magnetic configurations as illustrated in Fig. S6 and S7.† As summarized in Table 1, the ligand becomes spin-polarized by gaining about one electron from the metal. The magnetism of $Ca(pyz)_2$ and $Sr(pyz)_2$ derives primarily from the N atoms located on the pyrazine rings, as indicated in Tables S3 and S4.† Fig. S6† demonstrates that $Ca(pyz)_2$ is nonmagnetic when the spin orientations of N atoms within the same pyrazine are arranged in opposite directions. Thus, the spin polarization is accounted for in terms of the pyrazine ring. Four magnetic states are constructed using the $D_4$ real space symmetry of $Ca(pyz)_2$ and $Sr(pyz)_2$, including altermagnetic, ferromagnetic, stripe antiferromagnetic, and nonmagnetic

Table 2 Magnetic energies with HSE06 functional (in meV per unit cell) of four different magnetic states relative to the ground altermagnetic state, along with the deduced magnetic exchange parameter ($J$, in meV) and magnetic anisotropy parameter ($D$, in μeV) of $Ca(pyz)_2$ and $Sr(pyz)_2$

| | $Ca(pyz)_2$ | $Sr(pyz)_2$ |
|---|---|---|
| Altermagnetic | 0 | 0 |
| Ferromagnetic | 15.4 | 11.7 |
| Stripe antiferromagnetic | 7.3 | 5.2 |
| Nonmagnetic | 1485.3 | 1532.0 |
| $J$ | 7.70 | 5.85 |
| $D$ | 0.21 | 0.95 |

states, as shown in Fig. S7.† Both $Ca(pyz)_2$ and $Sr(pyz)_2$ prefer the altermagnetic state, where adjacent organic ligands tend to be arranged in antiparallel with each other (Fig. 2a). The energy differences between the altermagnetic and other magnetic states are summarized in Table 2.

Fig. S8† displays the total and atomically resolved density of states (DOS, $g(\mathscr{E})$) of the altermagnetic 2D MOFs. Both $Ca(pyz)_2$ and $Sr(pyz)_2$ are semiconductors with band gap values of 1.81 and 1.79 eV, respectively (Fig. 2e and S9†). The DOS around the Fermi level ($\mathscr{E}_F$) is mainly contributed by the $p_z$ orbitals of N and C atoms, while the contribution from metal atoms is negligible, as shown in Fig. S8.† This can also be confirmed by the orbital-resolved band structures, as shown in Fig. S10.† To further understand the altermagnetic exchange, band centers ($\mathscr{E}$) are calculated as

$$\epsilon = \frac{\int_{-\infty}^{\mathscr{E}_F} \mathscr{E} \times g(\mathscr{E})\mathrm{d}\mathscr{E}}{\int_{-\infty}^{\mathscr{E}_F} g(\mathscr{E})\mathrm{d}\mathscr{E}}. \quad (2)$$

It is shown that in 2D MOFs, the exchange of N's p orbitals contributes to the magnetic exchange parameters ($J$), resulting in an antiparallel alignment between adjacent ligands. For metal atoms without magnetism, there is almost no electron population on d orbitals, so there is no superexchange interactions mediated by them (Fig. S11†). The $J$ values are small due to the weak π-interaction between pyrazine ligands (Table 2), resulting in altermagnetic transition temperatures of 15.5 K for $Ca(pyz)_2$ and 11.5 K for $Sr(pyz)_2$ (Fig. S12†). These values are lower than that of the altermagnetic metal $RuO_2$ containing d electrons (400 K),[4,13,43] but higher than that of $\kappa$-$(BETS)_2FeBr_4$ (2.5 K).[44]

## Symmetries, spin-splitting, and valley-dependent spin polarization

As depicted in Fig. 2a, the unit cell of 2D $Ca(pyz)_2$ altermagnet consists of four magnetic pyrazine ligands. There is no inversion center between the sites occupied by the magnetic atoms from the opposite-spin sublattices. Based on the identification theories of spin point groups,[45] it is shown that in $Ca(pyz)_2$, the opposite spin sublattices are linked by a $C_{4z}$ transformation without any translation. The real-space crystallographic point group is $\mathbf{G} = 4/mmm$ and the molecular point group of the sublattice is $\mathbf{H} = mmm$. Thus, the nontrivial spin Laue group, which represents the spin–momentum locking in the altermagnetic phase can be decomposed as follows:

$$^{2}4/^{1}m^{1}m^{2}m = [E\|mmm] + [C_2\|C_{4z}][E\|mmm], \quad (3)$$

where the superscript on the upper left corner indicates the symmetry of the magnetic state at that place. The spin–momentum locking in altermagnetic 2D $Ca(pyz)_2$ and $Sr(pyz)_2$ is protected by the $^{2}4/^{1}m^{1}m^{2}m$ (#15.8.193) spin symmetry, which shows an anisotropy characterized by $d$-wave symmetry ($d_{xy}$) and two spin-degenerate nodal surfaces that pass through the $k$-point Γ (Γ–X and Γ–X′ in Fig. 2d).[3] Based on eqn (3), $T$-symmetry is broken due to the absence of $E$ in the coset $4/mmm \ominus mmm$.[3] The lifted spin degeneracies in the altermagnetic phase are allowed for crystal momenta ($\mathbf{k}$) and follow the equation $A\mathbf{H}\mathbf{k} = \mathbf{k}' \neq \mathbf{k}$, which leads to split energy isosurfaces ($\mathscr{E}$) from spin up and spin down states with an equal number (Fig. 2d–f). Consequently, the spin ($s$) and $\mathbf{k}$-dependent bands are represented as

$$\mathscr{E}(s,\mathbf{k}) = [C_2\|A\mathbf{H}]\mathscr{E}(s,\mathbf{k}) = \mathscr{E}(-s,\mathbf{k}') \quad (4)$$

Note that spin-splitting only occurs on paths of spin channel arrangements, *i.e.*, Γ–(Σ)–M for spin up and Γ–(Σ′)–M′ for spin down.[4] Fig. S13† displays the HSE06 band structures including SOC of 2D $Ca(pyz)_2$ and $Sr(pyz)_2$. For both 2D MOFs with light elements, SOC has no contribution to spin-splitting, ruling out the SOC-induced weak ferromagnetism.[27,46]

Additionally, $Ca(pyz)_2$ can be also manually constructed in a $P4/nmm$ (#129) phase based on the symmetry, with the $C_{4z}$ rotation axis located at the edge center of the tetragonal lattice (Fig. S14a and Table S5†). This phase also satisfies the symmetry conditions for exhibiting altermagnetism. The distinctive spin-splitting nature can be observed in its energy band (Fig. S14b†). However, the $P4/nmm$ (#129) phase of $Ca(pyz)_2$ is found to be dynamically unstable (Fig. S14c†).

To summarize, the energy band of altermagnetic $Ca(pyz)_2$ split in opposite directions along the Γ–(Σ)–M (red line in Fig. 2d) and M′–(Σ′)–Γ (blue line in Fig. 2d) path directions is opposite, leading to zero magnetization and non-polarization for $Ca(pyz)_2$ and $Sr(pyz)_2$ externally, as shown in Fig. 2f. Fig. 2g demonstrates that the sublattice in the altermagnetic 2D $Ca(pyz)_2$, which possesses a specific momentum space valley exhibiting spin-polarization. The spin polarizations of different valleys lead to equal but opposite DOS, where $g_+(\alpha) \neq g_-(\alpha)$, $g_+(\beta) \neq g_-(\beta)$, and $g_\pm(\alpha) = g_\mp(\beta)$, with the symbol "+" and "−" denoting spin up and down, respectively.

## Topological points and lines

Fig. 2f displays a trivial nodal point at the $k$-point X in the energy band around CBM with a zero Chern number protected by a 2D irreps $\bar{X}_3 \oplus \bar{X}_4$ in little group $2/m$,[47] and the spin-splitting states along the Γ–(Σ)–M path leads to a narrow energy gap of 3.57 meV in $Ca(pyz)_2$. A topological line is formed along the X–X′ path with a small gap at the mean value of 1.95 meV (Fig. 3a and S15†). Similar topological properties can also be presented in $Sr(pyz)_2$ (Fig. S16†). The movable nodal line of altermgnetic 2D

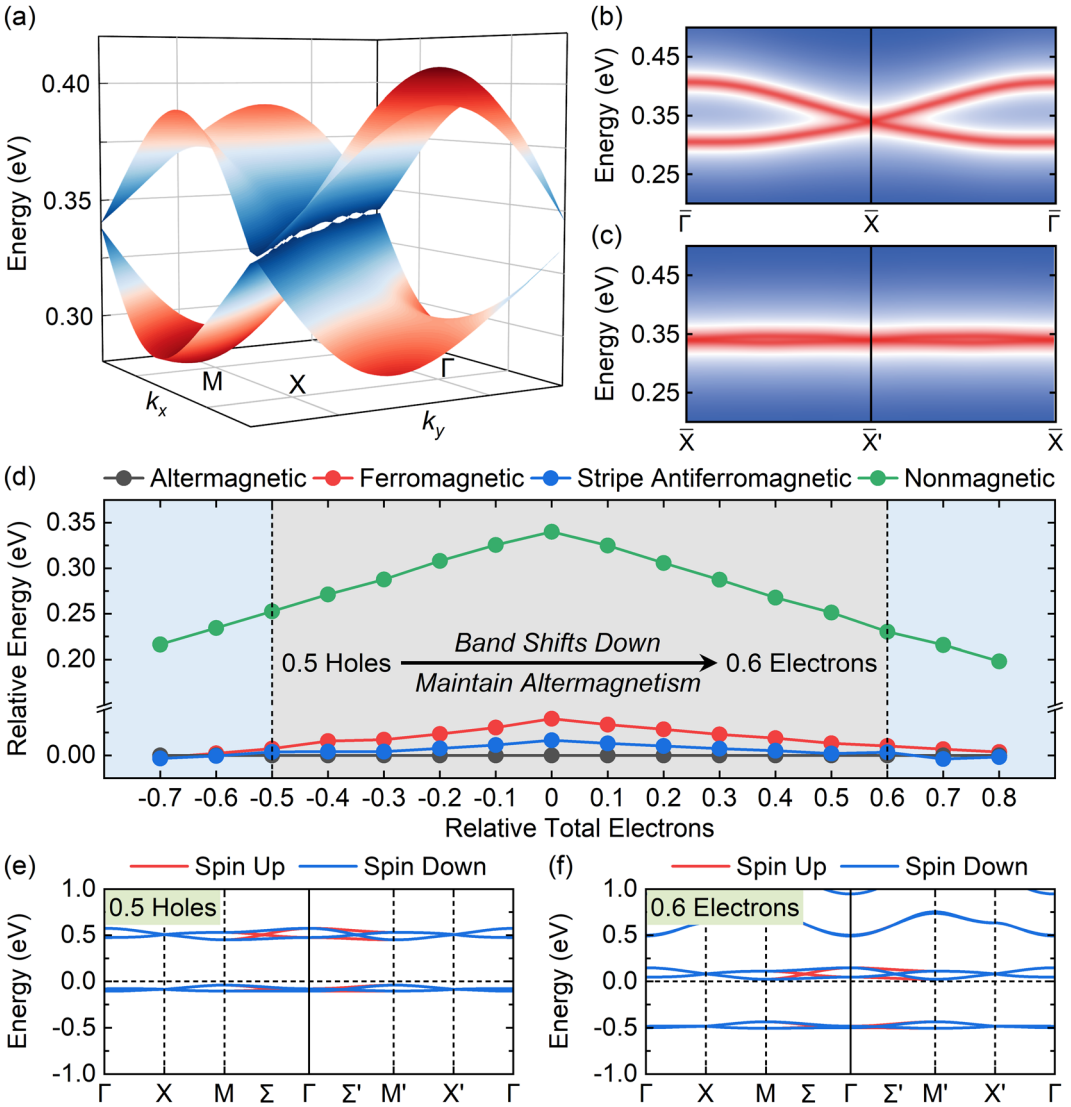


Fig. 3 Topological points and lines in the altermagnetic 2D $Ca(pyz)_2$. (a) Σ-centered 3D energy band structure of the altermagnetic spin-splitting near CBM for $Ca(pyz)_2$. (b and c) Topological edge states on the (b) (100) and (c) (110) surfaces of BZ for $Ca(pyz)_2$, where the $k$-points $\bar{\Gamma}$, $\bar{X}$, and $\bar{X}'$ are the corresponding projections along the surfaces of BZ. The red color indicates a higher state along the edge. (d) Relative energy difference of different magnetic states according to altermagnetic phase when doping with electrons or holes. The altermagentic ground state can be maintained within a doping range of up to 0.5 holes and 0.6 electrons (gray shadow). When the range of 0.2 electrons or holes is exceeded, the ground state becomes stripe antiferromagnetic (blue shadows). (e and f) Band structures of doping with (e) 0.5 holes and (f) 0.6 electrons around $\mathscr{E}_F$. By doping with electrons, the topological points and lines above $\mathscr{E}_F$ can move downwards towards the vicinity of $\mathscr{E}_F$, with an opposite direction when doping with holes. The topological properties are investigated with PBE functional and $\mathscr{E}_F$ is set to 0 eV.

MOFs is protected by the magnetic space group $P4'/nbm'$ (#125.367).[48] To confirm the existence of the nodal point at the $k$-point X, the edge states along the (100) and (110) directions of the first Brillouin zone (BZ) are calculated using the tight-binding approximation (TBA). The TBA Hamiltonian is derived from the p orbitals of N and C which contribute the most band structure around the Fermi level ($\mathscr{E}_F$), as shown in Fig. S17 and S18.† Fig. 3b, c, and S16† display a quadruple degenerate Dirac cone edge state that is evident at the projected $k$-point $\bar{X}$ in 2D MOFs. On the $\bar{X}$–$\bar{X}'$ path, a topological line is observed with a negligible gap. The existence of topological points and lines can give rise to remarkable physical properties, such as the anomalous Hall effect and transportation.[49,50]

Regulations of doping with electrons and holes in $Ca(pyz)_2$ are displayed in Fig. 3d–f, S19, and Table S6.† As shown in Fig. 3d and Table S6,† the relative energy difference according to altermagnetic phase decreases when more electrons or holes are doped. The altermagnetism ground state of $Ca(pyz)_2$ can be maintained within a doping range of up to 0.5 holes and 0.6 electrons. When the range of 0.2 electrons or holes is exceeded, the ground state turns into stripe antiferromagnetic. Fig. S19† displays altermagnetic band structures of doping with different amounts of electrons and holes. When doping with holes, the energy band moves upwards as a whole, and the valence band moves near the $\mathscr{E}_F$ (Fig. 3e). When doping with electrons, the band moves downwards, and the conduction band along with

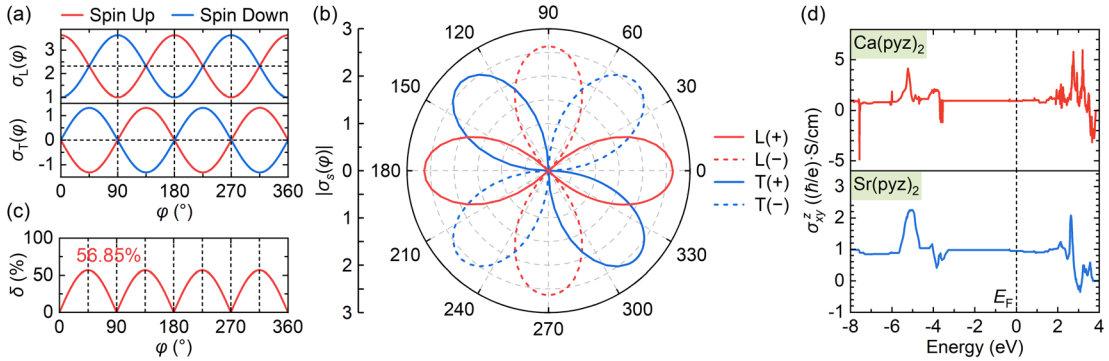


Fig. 4 Anisotropic charge and spin current and spin-current conversion ratio in the altermagnetic 2D MOFs. (a) Angle-dependent anisotropy of the longitudinal (L, top panel) and transverse (T, bottom panel) conductivities ($\sigma$) contributed from spin up and down pyrazine ligands with the electric field direction ($\varphi$) as mentioned in Fig. 1c–e. The relative values of conductivities are taken near CBM of Ca(pyz)$_2$. The total transverse charge current ($\sigma_T$) is always zero due to the opposite contributions from different spins. (b) Angle-dependent anisotropy of the longitudinal and transverse spin conductivities ($\sigma_s$) with the alternation in cycles of 45°, where the solid and dashed lines represent the positive and negative values of $\sigma$. (c) Spin-current conversion ratio ($\delta$) as a trigonometric function of $\varphi$, with the maximal value of 56.85% for Ca(pyz)$_2$ at 45°. (d) Spin Hall conductivities of altermagnetic 2D MOFs where $\mathscr{E}_F$ is set to 0 eV.

topological points and lines moves near the $\mathscr{E}_F$ (Fig. 3f). Band edges further proves that the topological points and lines around CBM still exists when doping with electrons and holes (Fig. S20†).

### Angle-dependent anisotropies and spin current

Further investigation is conducted to examine the anisotropic behavior of mechanical, magnetic, and electrical properties of Ca(pyz)$_2$ and Sr(pyz)$_2$. Young's modulus and Poisson's ratio of Ca(pyz)$_2$ and Sr(pyz)$_2$ display anisotropy in relation to angle, as shown in Fig. S21 and S22.† The Young's modulus values of Ca(pyz)$_2$ and Sr(pyz)$_2$ are 38.91 and 30.06 N m$^{-1}$, equivalent to 162.80 and 136.02 GPa by using sheet thickness, respectively. These values are comparable to those of the inorganic monolayers $\alpha$-P (164 GPa)[51] and $MoS_2$ (270 ± 100 GPa),[52] and larger to the value of Cr(tdz)$_2$ sheet (39 GPa).[38] Sr(pyz)$_2$ has a minimal Poisson's ratio of zero, which suggests its excellent resistance to fracture and resilience.

Magnetic anisotropy energy (MAE) values reveal the preferred direction of magnetization in the ground state and demonstrate the relative resistance of the long-range magnetic order to thermal disturbance at temperatures above zero. Table S7† summarized that the easy axes of the altermagnetic 2D Ca(pyz)$_2$ and Sr(pyz)$_2$ are both orientated out-of-plane with the corresponding MAE values of 0.21 and 0.95 μeV per unit cell.

The conductivities in the longitudinal and transverse directions exhibit periodic oscillation in response to the steady in-plane $\boldsymbol{E}$ direction. This results in the generation of an anisotropic spin current ($\boldsymbol{J}_s$, see details in ESI Note S2†). Using the classic Boltzmann transport theory and nearly free electron model, the energy ($\mathscr{E}$) of the band edge in a 2D gapped system can be expressed as

$$\mathscr{E} = \frac{\hbar^2}{2m_1}{k_x}^2 + \frac{\hbar^2}{2m_2}{k_y}^2, \tag{5}$$

where $m_1$ and $m_2$ are the effective masses in the $k_x$ and $k_y$ directions. The charge ($\boldsymbol{\sigma}$) and spin ($\boldsymbol{\sigma}_s$) conductivity tensors for an in-plane $\boldsymbol{E}$ along $\varphi$ direction in M(pyz)$_2$ (M = Ca and Sr) can be derived as

$$\boldsymbol{\sigma} = \boldsymbol{\sigma}_\alpha + \boldsymbol{\sigma}_\beta = \frac{ne^2\tau}{m_1 m_2}\begin{bmatrix} m_1 + m_2 & 0 \\ 0 & m_1 + m_2 \end{bmatrix} \tag{6}$$

and

$$\boldsymbol{\sigma}_s = \boldsymbol{\sigma}_\alpha - \boldsymbol{\sigma}_\beta = \frac{(m_1 - m_2)ne^2\tau}{m_1 m_2}\begin{bmatrix} -\cos(2\varphi) & \sin(2\varphi) \\ \sin(2\varphi) & \cos(2\varphi) \end{bmatrix}, \tag{7}$$

where $\boldsymbol{\sigma}_\alpha$ and $\boldsymbol{\sigma}_\beta$ are the conductivity originating from different spins, and $n$ and $\tau$ denote carrier density and relaxation time, respectively, which are assumed constant at 0 K (see details in ESI Note S2†).

As shown in Fig. 4a, the longitudinal charge current remains constant, with angle-dependent $\boldsymbol{J}_\alpha$ and $\boldsymbol{J}_\beta$. In contrast, the transverse charge current continuously remains at zero, confirming the absence of Hall charge current in M(pyz)$_2$. In Fig. 4b, the alternating period of longitudinal and transverse $\boldsymbol{J}_s$ is 45°, as indicated by the red and blue lines. The longitudinal and transverse $\boldsymbol{J}_s$ exhibit alternative positive and negative values every 90° with a phase difference of 45°, as indicated by the solid and dashed lines of each color. When an in-plane $\boldsymbol{E}$ is applied along a certain spin valley configuration of $\alpha$ or $\beta$, the resulting $\boldsymbol{J}_s$ will be longitudinal and will flow in the opposite direction depending on the spin types along which $\boldsymbol{E}$ is applied. When $\boldsymbol{E}$ is applied at the angular bisector of two spin arrangements, carriers with $\alpha$ and $\beta$ spins will undergo equal deflection but in opposite directions. This leads to the generation of SHE and pure transverse $\boldsymbol{J}_s$ with no Hall charge current ($\boldsymbol{J}$). The charge–spin conversion ratio ($\delta$) achieves its maximal value of $\delta = \left|\frac{\sigma_{s,xy}}{\sigma_{xx}}\right| = \left|\frac{m_1 - m_2}{m_1 + m_2}\right|$. Based on the spin-splitting from eqn (4) and anisotropy analysis, it is found that the effective mass in the $k_x$ direction ($m^*_{xx}$) of $\alpha$ valley is equal to that in the $k_y$ direction ($m^*_{yy}$) of $\beta$ valley, and $m^*_{yy}$ of $\alpha$ valley is

equal to $m_{xx}^{*}$ of $\beta$ valley. By fitting the band structure with a quadratic function from the $k$-point M to $\Sigma'$ and $\Sigma$ (Fig. 2d), we can determine the proportions of charge and spin currents from up and down spins, as well as the value of $\delta$ (Fig. S23†). The calculated $\delta$ of $M(pyz)_2$ varies with angle, showing a periodicity of 45°. The largest $\delta$ values observed are 56.85% for $Ca(pyz)_2$ and 86.04% for $Sr(pyz)_2$ (Fig. 4c, and see details in ESI Note S2†). The corresponding angles between the two spin transport channels are 59.24° and 84.42°, respectively, which are significantly greater than those reported from SOC (12% for $\beta$-Ta (ref. 53) and 30% for $\beta$-W/CoFeB (ref. 54)), as well as higher than the values of recently reported altermagnets (28% for $RuO_2$ (ref. 8) and 70% for $V_2Se_2O$ (ref. 22)). Fig. 4d displays the spin Hall conductivity (SHC) calculated by Kubo formula with Qiao method (see details in Methods and ESI Note S2†).[55] The semiconducting MOFs with light elements have a largest SHC value of $10^0$ to $10^1$ $\hbar$ $e^{-1}$ S $cm^{-1}$ at about 3 eV above $\mathscr{E}_F$. It is important to emphasize that $\boldsymbol{J}_s$ is consistently found in $M(pyz)_2$ (M = Ca and Sr), and the pure $\boldsymbol{J}_s$ is aligned in a specific $E$ direction.

## Conclusions

In summary, we report two 2D MOFs, namely $M(pyz)_2$ (M = Ca and Sr), which possess an altermagnetic ground state. These MOFs exhibit unique properties, including non-degenerate spins within zero macroscopic moments, π-magnetism, topological points and lines, and angle-dependent anisotropies by using first-principles calculations and group theory. It is demonstrated that magnetism is contributed by pyrazine rings in a certain arrangement, forming a magnetic symmetry of ${}^{2}4/{}^{1}m^{1}m^{2}m$ (#15.8.193), which leads to the broken $T$-symmetry and spin-polarized bands in reciprocal momentum space. Both $Ca(pyz)_2$ and $Sr(pyz)_2$ are semiconductors with band gaps of 1.81 and 1.79 eV, respectively. An electric-field-controlled spin current can be achieved by making use of the anisotropic in-plane spin distribution. In particular, the spin Hall effect generates a pure spin current when an electric field is applied along the angular bisector of two spin configurations. Our study presents a rational design strategy to achieve multifunctional altermagnets based on 2D MOFs with electric-field-controlled spin currents.

## Methods

The first-principles calculations are performed by density functional theory (DFT)[56] implemented in the Vienna *Ab initio* Simulation Package (VASP).[57,58] The DFT-D3 approach with the Becke–Johnson damping function is applied for the π–π type van der Waals (vdW) interactions between the neighboring pyrazine rings around the metal atoms.[59,60] The Perdew–Bruke–Ernzerhof (PBE) functional[61] is adopted in geometric optimization and the corrected Heyd–Scuceria–Ernzerhof (HSE06) hybrid functional[62] is applied for describing the 2D band structure and density of states. The projector augmented-wave (PAW) pseudopotential[63,64] is employed with the plane-wave energy cutoff of 500 eV. Monkhorst–Pack $k$-point meshes of $6 \times 6 \times 1$ are investigated for structure optimization and property calculations with the convergence criteria of energy and force of $10^{-6}$ eV and 0.01 eV $Å^{-1}$, respectively.[65] Bader charge analyses are investigated to characterize the charge transfer between the metal atoms and pyrazine ligands.[66–70] Spin–orbit coupling (SOC) is considered non-self-consistently for different spin orientations in the magnetic anisotropy energy (MAE) calculations with the energy convergence criteria of $10^{-8}$ eV, which is calculated as $MAE = E_{[100]} - E_{[001]}$.[71] The 3D band structure is carried out *via* the PBE functional with the grid spacing of $1.85 \times 10^{-3}$ $Å^{-1}$, corresponding to the Monkhorst–Pack $k$-point meshes of $50 \times 50 \times 1$ in a reciprocal unit cell.[65] The edge states are performed using the WannierTools[72] code based on the tight-binding approximation (TBA) model constructed by Wannier90,[73,74] where the p orbitals of N and C are investigated to simulate the TBA Hamiltonian, including a total of 72 bands of frozen window. The topological Chern numbers and band irreducible representations are calculated by VASPBERRY[75] and IrRep package,[76] respectively. The spin Hall conductivity (SHC) is calculated by the Kubo formula with the Qiao method[55] implemented in Wannier90 with Berry $k$-point meshes of $25 \times 25 \times 1$. All structures obtain a vacuum layer with a thickness of at least 15 Å to avoid mirror interactions between periodic layers.

To investigate the dynamic and thermal stabilities, phonon spectra are simulated within the density functional perturbation theory (DFPT)[77,78] by the Phonopy code,[79–81] and *ab initio* molecular dynamic (AIMD) simulations are performed for 5 ps with the time step of 1 fs at 300, 600, and 900 K in the canonical (NVT) ensemble by using Nose–Hoover thermostats.[82–85] All calculations are performed in the $2 \times 2 \times 1$ supercell with 168 atoms and the $k$-meshes of $3 \times 3 \times 1$ and $1 \times 1 \times 1$ are investigated in the phonon spectrum and AIMD simulations, respectively. The acoustic sum rule is included in phonon spectrum calculations to cure the tiny imaginary frequencies of pure translations.

The mechanical stability and properties are calculated with the stress–strain method.[42] For a tetragonal 2D crystal in the linear elastic region, the stress–strain ($\sigma$–$\varepsilon$) relationship follows Hooke's law and can be represented by the Voigt notation, *i.e.*,

$$\begin{bmatrix} \sigma_1 \\ \sigma_2 \\ \sigma_3 \end{bmatrix} = \begin{bmatrix} C_{11} & C_{12} & 0 \\ C_{12} & C_{11} & 0 \\ 0 & 0 & C_{66} \end{bmatrix} \begin{bmatrix} \varepsilon_1 \\ \varepsilon_2 \\ \varepsilon_3 \end{bmatrix}, \quad (8)$$

where $C_{11}$, $C_{12}$, and $C_{66}$ are the second-order in-plane elastic constants. In order to calculate the $C_{ij}$ values, the strain range $-2\% \leq \Delta\varepsilon \leq 2\%$ with the increment of 0.5% is investigated. The elastic stability conditions of a tetragonal 2D crystal is $C_{11} > 0$, $C_{66} > 0$, and $C_{11} > |C_{12}|$.[42] The Young's modulus and Poisson's ratio are implemented with the VASPKIT code.[86]

The estimated magnetic transition temperature is performed by the Monte Carlo simulation based on the Heisenberg model with a $24 \times 24 \times 1$ supercell and a temperature step of 0.5 K from 1 to 50 K, as implemented in the SEU-mtc package.[87] Due to the $D_4$ symmetry and the magnetism completely

provided by the pyrazine rings, the spin Hamiltonian ($H$) can be expressed as

$$H = J\sum_{\langle i,j\rangle} S_i S_j + DS_z{}^2, \quad (9)$$

where $J$ and $S = 1/2$ represent the nearest neighbor exchange parameter and the unit spin vector along the $c$-axis, respectively. For $M(pyz)_2$ (M = Ca and Sr), $J = (\mathscr{E}_{FM} - \mathscr{E}_{AM})/2$. $D$ denotes the magnetic anisotropy parameter calculated from the MAE value per pyrazine ligand. For $M(pyz)_2$ (M = Ca and Sr), $DS^2$ = MAE/4.

The anisotropy of spin conductivities is derived based on the theories in solid state physics and condensed matter with the DFT calculations of band structures, and more derivation details are summarized in ESI Note S2.†

## Data availability

The data supporting the findings of this study are available within the article and its ESI.†

## Author contributions

Y. C. carried out the calculations, derivations, and visualizations. H. L. and X. W. convinced the idea and supervised the work. All authors discussed the results and contributed to the manuscript.

## Conflicts of interest

There are no conflicts to declare.

## Acknowledgements

This research is supported by the National Natural Science Foundation for Distinguished Young Scholars (Grant No. 22225301), the National Natural Science Foundation of China (Grant No. 22303092), the Strategic Priority Research Program of the Chinese Academy of Sciences (Grant No. XDB0450101), the Innovation Program for Quantum Science and Technology (Grant No. 2021ZD0303302), the National College Student Innovation and Entrepreneurship Training Program (Grant No. 202110358035), and Super Computer Center of USTCSCC and SCCAS.

## References

1 S. A. Wolf, D. D. Awschalom, R. A. Buhrman, J. M. Daughton, S. von Molnár, M. L. Roukes, A. Y. Chtchelkanova and D. M. Treger, *Science*, 2001, **294**, 1488–1495.
2 X. Li, X. Wu, Z. Li and J. Yang, *Phys. Rev. B: Condens. Matter Mater. Phys.*, 2015, **92**, 125202.
3 L. Šmejkal, J. Sinova and T. Jungwirth, *Phys. Rev. X*, 2022, **12**, 031042.
4 L. Šmejkal, J. Sinova and T. Jungwirth, *Phys. Rev. X*, 2022, **12**, 040501.
5 I. Mazin and T. P. R. X. Editors, *Phys. Rev. X*, 2022, **12**, 040002.
6 I. Mazin, *Physics*, 2024, **17**, 4.
7 L. Šmejkal, A. B. Hellenes, R. González-Hernández, J. Sinova and T. Jungwirth, *Phys. Rev. X*, 2022, **12**, 011028.
8 R. González-Hernández, L. Šmejkal, K. Výborný, Y. Yahagi, J. Sinova, T. Jungwirth and J. Železný, *Phys. Rev. Lett.*, 2021, **126**, 127701.
9 I. I. Mazin, K. Koepernik, M. D. Johannes, R. González-Hernández and L. Šmejkal, *Proc. Natl. Acad. Sci. U. S. A.*, 2021, **118**, e2108924118.
10 R. D. Gonzalez Betancourt, J. Zubáč, R. Gonzalez-Hernandez, K. Geishendorf, Z. Šobáň, G. Springholz, K. Olejník, L. Šmejkal, J. Sinova, T. Jungwirth, S. T. B. Goennenwein, A. Thomas, H. Reichlová, J. Železný and D. Kriegner, *Phys. Rev. Lett.*, 2023, **130**, 036702.
11 S. Bhattacharjee, E. Bousquet and P. Ghosez, *Phys. Rev. Lett.*, 2009, **102**, 117602.
12 Q. Si, R. Yu and E. Abrahams, *Nat. Rev. Mater.*, 2016, **1**, 16017.
13 L. Šmejkal, R. González-Hernández, T. Jungwirth and J. Sinova, *Sci. Adv.*, 2020, **6**, eaaz8809.
14 Z. Feng, X. Zhou, L. Šmejkal, L. Wu, Z. Zhu, H. Guo, R. González-Hernández, X. Wang, H. Yan, P. Qin, X. Zhang, H. Wu, H. Chen, Z. Meng, L. Liu, Z. Xia, J. Sinova, T. Jungwirth and Z. Liu, *Nat. Electron.*, 2022, **5**, 735–743.
15 T. Tschirner, P. Keßler, R. D. Gonzalez Betancourt, T. Kotte, D. Kriegner, B. Büchner, J. Dufouleur, M. Kamp, V. Jovic, L. Šmejkal, J. Sinova, R. Claessen, T. Jungwirth, S. Moser, H. Reichlova and L. Veyrat, *APL Mater.*, 2023, **11**, 101103.
16 H. Bai, Y. C. Zhang, Y. J. Zhou, P. Chen, C. H. Wan, L. Han, W. X. Zhu, S. X. Liang, Y. C. Su, X. F. Han, F. Pan and C. Song, *Phys. Rev. Lett.*, 2023, **130**, 216701.
17 A. Bose, N. J. Schreiber, R. Jain, D. Shao, H. P. Nair, J. Sun, X. S. Zhang, D. A. Muller, E. Y. Tsymbal, D. G. Schlom and D. C. Ralph, *Nat. Electron.*, 2022, **5**, 267–274.
18 H. Bai, L. Han, X. Y. Feng, Y. J. Zhou, R. X. Su, Q. Wang, L. Y. Liao, W. X. Zhu, X. Z. Chen, F. Pan, X. L. Fan and C. Song, *Phys. Rev. Lett.*, 2022, **128**, 197202.
19 S. Karube, T. Tanaka, D. Sugawara, N. Kadoguchi, M. Kohda and J. Nitta, *Phys. Rev. Lett.*, 2022, **129**, 137201.
20 Y. Jiang, Z. Wang, K. Samanta, S. Zhang, R. Xiao, W. J. Lu, Y. P. Sun, E. Y. Tsymbal and D. Shao, *Phys. Rev. B: Condens. Matter Mater. Phys.*, 2023, **108**, 174439.
21 P. W. Anderson, *Science*, 1987, **235**, 1196–1198.
22 H. Ma, M. Hu, N. Li, J. Liu, W. Yao, J. Jia and J. Liu, *Nat. Commun.*, 2021, **12**, 2846.
23 X. Chen, D. Wang, L. Li and B. Sanyal, *Appl. Phys. Lett.*, 2023, **123**, 022402.
24 Z. Gao, S. Qu, B. Zeng, Y. Liu, J. Wen, H. Sun, P. Guo and Z. Lu, *arXiv*, 2023, preprint, arXiv:2311.04418.
25 J. Sødequist and T. Olsen, *Appl. Phys. Lett.*, 2024, **124**, 182409.
26 L. Bai, W. Feng, S. Liu, L. Šmejkal, Y. Mokrousov and Y. Yao, *arXiv*, 2024, preprint, arXiv:2406.02123.
27 J. Krempaský, L. Šmejkal, S. W. D'Souza, M. Hajlaoui, G. Springholz, K. Uhlířová, F. Alarab, P. C. Constantinou,

V. Strocov, D. Usanov, W. R. Pudelko, R. González-Hernández, A. Birk Hellenes, Z. Jansa, H. Reichlová, Z. Šobáň, R. D. Gonzalez Betancourt, P. Wadley, J. Sinova, D. Kriegner, J. Minár, J. H. Dil and T. Jungwirth, *Nature*, 2024, **626**, 517–522.

28 Y. Zhu, X. Chen, X. Liu, Y. Liu, P. Liu, H. Zha, G. Qu, C. Hong, J. Li, Z. Jiang, X. Ma, Y. Hao, M. Zhu, W. Liu, M. Zeng, S. Jayaram, M. Lenger, J. Ding, S. Mo, K. Tanaka, M. Arita, Z. Liu, M. Ye, D. Shen, J. Wrachtrup, Y. Huang, R. He, S. Qiao, Q. Liu and C. Liu, *Nature*, 2024, **626**, 523–528.

29 O. Fedchenko, J. Minár, A. Akashdeep, S. W. D'Souza, D. Vasilyev, O. Tkach, L. Odenbreit, Q. Nguyen, D. Kutnyakhov, N. Wind, L. Wenthaus, M. Scholz, K. Rossnagel, M. Hoesch, M. Aeschlimann, B. Stadtmüller, M. Kläui, G. Schönhense, T. Jungwirth, A. B. Hellenes, G. Jakob, L. Šmejkal, J. Sinova and H. Elmers, *Sci. Adv.*, 2024, **10**, eadj4883.

30 H. Zhou, J. R. Long and O. M. Yaghi, *Chem. Rev.*, 2012, **112**, 673–674.

31 J. A. Real, G. De Munno, M. C. Munoz and M. Julve, *Inorg. Chem.*, 1991, **30**, 2701–2704.

32 H. N. Bordallo, L. Chapon, J. L. Manson, J. Hernández-Velasco, D. Ravot, W. M. Reiff and D. N. Argyriou, *Phys. Rev. B: Condens. Matter Mater. Phys.*, 2004, **69**, 224405.

33 H. Sun, B. Ma, S. Gao and G. Su, *Chem. Commun.*, 2001, **37**, 2586–2587.

34 X. Li and J. Yang, *J. Am. Chem. Soc.*, 2019, **141**, 109–112.

35 P. Perlepe, I. Oyarzabal, A. Mailman, M. Yquel, M. Platunov, I. Dovgaliuk, M. Rouzières, P. Négrier, D. Mondieig, E. A. Suturina, M.-A. Dourges, S. Bonhommeau, R. A. Musgrave, K. S. Pedersen, D. Chernyshov, F. Wilhelm, A. Rogalev, C. Mathonière and R. Clérac, *Science*, 2020, **370**, 587–592.

36 X. Li, H. Lv, X. Liu, T. Jin, X. Wu, X. Li and J. Yang, *Sci. China: Chem.*, 2021, **64**, 2212–2217.

37 H. Lv, X. Li, D. Wu, Y. Liu, X. Li, X. Wu and J. Yang, *Nano Lett.*, 2022, **22**, 1573–1579.

38 X. Li, Q. Liu, Y. Tang, W. Li, N. Ding, Z. Liu, H. Fu, S. Dong, X. Li and J. Yang, *J. Am. Chem. Soc.*, 2023, **145**, 7869–7878.

39 J. Sinova, S. O. Valenzuela, J. Wunderlich, C. H. Back and T. Jungwirth, *Rev. Mod. Phys.*, 2015, **87**, 1213–1260.

40 M. Naka, S. Hayami, H. Kusunose, Y. Yanagi, Y. Motome and H. Seo, *Nat. Commun.*, 2019, **10**, 4305.

41 Y. Luo, S. Bag, O. Zaremba, A. Cierpka, J. Andreo, S. Wuttke, P. Friederich and M. Tsotsalas, *Angew. Chem., Int. Ed.*, 2022, **61**, e202200242.

42 V. Wang, G. Tang, Y. Liu, R. Wang, H. Mizuseki, Y. Kawazoe, J. Nara and W. T. Geng, *J. Phys. Chem. Lett.*, 2022, **13**, 11581–11594.

43 K. H. Ahn, A. Hariki, K. W. Lee and J. Kuneš, *Phys. Rev. B*, 2019, **99**, 184432.

44 H. Fujiwara, E. Fujiwara, Y. Nakazawa, B. Z. Narymbetov, K. Kato, H. Kobayashi, A. Kobayashi, M. Tokumoto and P. Cassoux, *J. Am. Chem. Soc.*, 2001, **123**, 306–314.

45 D. Litvin, *Acta Crystallogr., Sect. A: Cryst. Phys., Diffr., Theor. Gen. Crystallogr.*, 1977, **33**, 279–287.

46 M. Milivojević, M. Orozović, S. Picozzi, M. Gmitra and S. Stavrić, *2D Mater.*, 2024, **11**, 035025.

47 B. Bradlyn, L. Elcoro, J. Cano, M. G. Vergniory, Z. Wang, C. Felser, M. I. Aroyo and B. A. Bernevig, *Nature*, 2017, **547**, 298–305.

48 H. Watanabe, H. C. Po and A. Vishwanath, *Sci. Adv.*, 2018, **4**, eaat8685.

49 N. Nagaosa, J. Sinova, S. Onoda, A. H. MacDonald and N. P. Ong, *Rev. Mod. Phys.*, 2010, **82**, 1539–1592.

50 W. Du, R. Peng, Z. He, Y. Dai, B. Huang and Y. Ma, *npj 2D Mater. Appl.*, 2022, **6**, 11.

51 Z. Zhuo, X. Wu and J. Yang, *J. Am. Chem. Soc.*, 2016, **138**, 7091–7098.

52 S. Bertolazzi, J. Brivio and A. Kis, *ACS Nano*, 2011, **5**, 9703–9709.

53 L. Liu, C. Pai, Y. Li, H. W. Tseng, D. C. Ralph and R. A. Buhrman, *Science*, 2012, **336**, 555–558.

54 C. Pai, L. Liu, Y. Li, H. W. Tseng, D. C. Ralph and R. A. Buhrman, *Appl. Phys. Lett.*, 2012, **101**, 122404.

55 J. Qiao, J. Zhou, Z. Yuan and W. Zhao, *Phys. Rev. B*, 2018, **98**, 214402.

56 R. G. Parr, *Annu. Rev. Phys. Chem.*, 1983, **34**, 631–656.

57 G. Kresse and J. Furthmüller, *Comput. Mater. Sci.*, 1996, **6**, 15–50.

58 G. Kresse and J. Furthmüller, *Phys. Rev. B: Condens. Matter Mater. Phys.*, 1996, **54**, 11169–11186.

59 S. Grimme, J. Antony, S. Ehrlich and H. Krieg, *J. Chem. Phys.*, 2010, **132**, 154104.

60 S. Grimme, S. Ehrlich and L. Goerigk, *J. Comput. Chem.*, 2011, **32**, 1456–1465.

61 J. P. Perdew, K. Burke and M. Ernzerhof, *Phys. Rev. Lett.*, 1996, **77**, 3865–3868.

62 A. V. Krukau, O. A. Vydrov, A. F. Izmaylov and G. E. Scuseria, *J. Chem. Phys.*, 2006, **125**, 224106.

63 P. E. Blöchl, *Phys. Rev. B: Condens. Matter Mater. Phys.*, 1994, **50**, 17953–17979.

64 G. Kresse and D. Joubert, *Phys. Rev. B: Condens. Matter Mater. Phys.*, 1999, **59**, 1758–1775.

65 H. J. Monkhorst and J. D. Pack, *Phys. Rev. B: Solid State*, 1976, **13**, 5188–5192.

66 R. Bader, *Atoms in Molecules: A Quantum Theory*, Oxford University Press, New York, 1990.

67 G. Henkelman, A. Arnaldsson and H. Jónsson, *Comput. Mater. Sci.*, 2006, **36**, 354–360.

68 E. Sanville, S. D. Kenny, R. Smith and G. Henkelman, *J. Comput. Chem.*, 2007, **28**, 899–908.

69 W. Tang, E. Sanville and G. Henkelman, *J. Phys.: Condens. Matter*, 2009, **21**, 084204.

70 M. Yu and D. R. Trinkle, *J. Chem. Phys.*, 2011, **134**, 064111.

71 C. Zener, *Phys. Rev.*, 1954, **96**, 1335–1337.

72 Q. Wu, S. Zhang, H. Song, M. Troyer and A. A. Soluyanov, *Comput. Phys. Commun.*, 2018, **224**, 405–416.

73 A. A. Mostofi, J. R. Yates, G. Pizzi, Y. S. Lee, I. Souza, D. Vanderbilt and N. Marzari, *Comput. Phys. Commun.*, 2014, **185**, 2309–2310.

74 G. Pizzi, V. Vitale, R. Arita, S. Blügel, F. Freimuth, G. Géranton, M. Gibertini, D. Gresch, C. Johnson,

T. Koretsune, J. Ibañez-Azpiroz, H. Lee, J. M. Lihm, D. Marchand, A. Marrazzo, Y. Mokrousov, J. I. Mustafa, Y. Nohara, Y. Nomura, L. Paulatto, S. Poncé, T. Ponweiser, J. Qiao, F. Thöle, S. S. Tsirkin, M. Wierzbowska, N. Marzari, D. Vanderbilt, I. Souza, A. A. Mostofi and J. R. Yates, *J. Phys.: Condens. Matter*, 2020, **32**, 165902.

75 H. J. Kim, *Zenodo*, 2018, 1402592.

76 M. Iraola, J. L. Mañes, B. Bradlyn, M. K. Horton, T. Neupert, M. G. Vergniory and S. S. Tsirkin, *Comput. Phys. Commun.*, 2022, **272**, 108226.

77 P. Giannozzi, S. de Gironcoli, P. Pavone and S. Baroni, *Phys. Rev. B: Condens. Matter Mater. Phys.*, 1991, **43**, 7231–7242.

78 X. Gonze and C. Lee, *Phys. Rev. B: Condens. Matter Mater. Phys.*, 1997, **55**, 10355–10368.

79 A. Togo and I. Tanaka, *Scr. Mater.*, 2015, **108**, 1–5.

80 A. Togo, L. Chaput, T. Tadano and I. Tanaka, *J. Phys.: Condens. Matter*, 2023, **35**, 353001.

81 A. Togo, *J. Phys. Soc. Jpn.*, 2023, **92**, 012001.

82 S. Nosé, *J. Chem. Phys.*, 1984, **81**, 511–519.

83 W. G. Hoover, *Phys. Rev. A*, 1985, **31**, 1695–1697.

84 S. Nosé, *Prog. Theor. Phys. Suppl.*, 1991, **103**, 1–46.

85 D. M. Bylander and L. Kleinman, *Phys. Rev. B: Condens. Matter Mater. Phys.*, 1992, **46**, 13756–13761.

86 V. Wang, N. Xu, J. Liu, G. Tang and W. Geng, *Comput. Phys. Commun.*, 2021, **267**, 108033.

87 Y. Zhang, B. Wang, Y. Guo, Q. Li and J. Wang, *Comput. Mater. Sci.*, 2021, **197**, 110638.